Surface Oxidation and Wettability of Fe–Mn and Fe–Mn–Si-Alloyed Steel After Annealing

YULIU YOU, JUNGKI KIM, CEES KWAKERNAAK [ID], JOHANNES C. BROUWER, RUUD WESTERWAAL, and WILLEM G. SLOOF [ID]

The surface oxidation and wettability of Mn and Si-alloyed steel after annealing at different conditions are studied with scanning electron microscope (SEM), X-ray photoelectron spectroscopy (XPS), and a so-called de-wetting method. After exposure at 950 °C for 1 hour in an Ar + 5 vol pct H_2 gas atmosphere with dew points (DP) ranging from – 40 °C to 10 °C, oxides were observed along the grain boundaries or dispersed on the surface for the Fe–1.8 Mn steels while a continuous oxides layer was formed on Fe–1.9 Mn–0.94 Si steels (composition in weight fractions). The oxides formed at different DPs were predicted based on thermodynamic calculations. (Fe,Mn)O was formed on Fe–1.8 Mn steel at the whole range of DPs, while the oxide phase on Fe–1.9 Mn–0.94 Si steel depends on the DP. At low-DP SiO_2 were formed and with increasing the DP $(Fe,Mn)SiO_3$ or $(Fe,Mn)SiO_3$ + $(Fe,Mn)_2SiO_4$ were formed and finally $(Fe,Mn)_2SiO_4$ were formed. An increase of the fraction of Fe in the oxide with increasing DP for both steels was observed with XPS analysis. As a measure for the surface wettability, the contact angle of Pb droplets on the annealed steels surfaces was determined with SEM and image analysis software. Also, the contact angle of Pb on pure Fe and on the Mn and Si alloyed steels free of surface oxides was measured for comparison. The results show that the contact angle of Pb on the steel surfaces after annealing decreases with increasing DP. This improved wettability with increasing dew point is related to the Fe fraction of the oxides formed on the surface.

I. INTRODUCTION

ADVANCED high strength steel (AHSS) with favourable combination of high strength, high ductility and improved crash worthiness allow automobiles to have lower weight without compromising safety.[1] Consequently, the fuel consumption and CO_2 footprint of the automobiles will be reduced which have certainly encouraged a broader application of AHSS in the automotive industry. With the development of the AHSS, new challenges arise for the galvanizing processes. The high contents of alloying elements such as Mn, Si, or Al in the AHSS, tend to segregate to the steel surface upon annealing and can be selectively oxidized prior to hot-dip galvanizing (HDG) because of their high affinity for oxygen.[2–5] These surface oxides, in particular, the amorphous MnO_2 or SiO_2 are detrimental to the wettability of AHSS, hindering the formation of a fully sealed inhibition layer during HDG[4–10] and may result in bare spots.[11–15] Consequently, the adhesion of the zinc coating to the steel substrate as well as protection against corrosion is diminished.[16–18] In order to solve this adhesion problem, it is imperative to study the relation between the surface oxide compositions and morphologies of AHSS annealed at different dew points and the wettability.

The wetting during hot-dip galvanizing of steel surfaces involves liquid zinc alloyed with a small amount of Al.[7] Then, an inhibition layer at the steel surfaces is formed composed of $Zn_xFe_2Al_5$ to mitigate the formation of Zn-Fe intermetallics. The Al in the Zn bath may also reduce oxides present at the steel surfaces by an aluminothermic reaction.[19,20] Various methods have been employed to study the reactive wetting of steels upon galvanizing.[21–23]

The transition from internal to external oxidation of Fe–Mn alloyed steels have been studied[24] and it was observed that increasing the annealing dew point promotes internal oxidation. The oxides phases formed on Fe–Mn–Cr alloyed steels also have been studied with

YULIU YOU, CEES KWAKERNAAK, JOHANNES C. BROUWER, and WILLEM G. SLOOF are with the Department of Materials Science and Engineering, Delft University of Technology, Mekelweg 2, 2628 CD, Delft, The Netherlands. Contact e-mail: youyuliu2022@gmail.com JUNGKI KIM is with the POSCO, 102-1604, 65, Nunso 4-gil, Gwangyang-si, Jeollanam-do, Republic of Korea. RUUD WESTERWAAL is with the Tata Steel Nederland Technology B.V., P.O. Box 1000, 1970 CA, IJmuiden, The Netherlands.

simulations and experiments[25,26] and showed that adding Cr to the Fe–Mn-based steel alloys results in the formation of $(Mn,Cr,Fe)_3O_4$ spinel during annealing. Increasing the Mn concentration in the alloy promotes the formation of $(Mn,Cr,Fe)_3O_4$ spinel and $(Fe,Mn)O$.

In this work, the phase diagrams of Fe–Mn binary and Fe–Mn–Si ternary steel alloys were calculated, the composition and morphology of the oxides formed in these steel alloys as a function of the dew point of the annealing ambient were studied by means of scanning electron microscopy (SEM), X-ray diffractometry (XRD), and X-ray photoelectron microscopy (XPS). To study the relation between wettability and surface condition of the steels after annealing, a so-called de-wetting method was employed. This method has been used previously to investigate the wettability of Cu,[27] Al,[28] and Ni.[29] Since the wetting of steel by liquid Zn is reactive,[11] Pb is used instead to study the wettability. Namely, Pb and Fe are mutually insoluble up to 1300 °C. Moreover, since the oxides at steel surfaces are more stable than that of PbO, their reduction by Pb is not likely. Hence, Pb was used as a probe to detect the nonreactive wetting of steel surfaces. The contact angle was determined of Pb droplets as a result of de-wetting of a Pb film applied on different steel surfaces after annealing. For comparison, the contact angles of several Pb droplets on bare pure Fe, Fe–Mn steel, and Fe–Mn–Si steel annealed in a reducing environment were also measured directly from cross sections prepared by plasma focussed ion beam technique.

II. EXPERIMENTAL

The chemical composition of the steels are listed in Table I. In addition, pure iron sheet (99.99 pct, Chempur, Germany) was also included in this research. Coupons of the steels and pure iron were cut by electro-discharge machining (EDM) with dimensions of $20 \times 10 \times 1$ mm. Prior to annealing, the surfaces of all specimens were ground with SiC emery paper and polished with diamond paste with 0.25 μm diamond grains in the final step.

The steel alloys and pure iron were then annealed in a horizontal quartz tube furnace (Carbolite MTF 12/38/850, UK) at 950 °C for 1 hour in a gas mixture of Ar + 5 vol pct H_2 (Linde gas, The Netherlands, A550H and H550, respectively) at atmospheric pressure. The quartz tube inner diameter was 30 mm and the total gas flow was 200 sccm. The evaporated de-aerated water (with resistivity of 18.2 MΩ cm at 25 °C, concentration of dissolved O_2 less than 100 ppb) was added to the gas

mixture to provide and maintain the required dew points in the range of -40 °C to $+10$ °C to create different surface oxide compositions and morphologies. The corresponding oxygen partial pressure was calculated using the formulae provided by Huin et al.[30]; see Table II. Details of the control and measurement of the dew point are explained elsewhere.[26] After annealing the samples were directly stored in isopropanol to avoid oxidation at room temperature in air. One series of samples was used for characterization and the second series of samples was used for de-wetting experiment. Thus, two steel samples were annealed simultaneously.

The composition of the surface oxides was analysed with X-ray photoelectron spectroscopy (XPS). The annealed steel sample was mounted on a sample holder while immersed with isopropanol. Next, the assembly introduced into the XPS load lock, which was pumped to ultra-high vacuum. With this procedure the sample was exposed less than one minute to air at room temperature. The photoelectron spectra were recorded with a PHI 5400 ESCA (Physical Instruments, USA) operated with an X-ray source operated at 200 W and 13 kV using an Al anode (Al K_α = 1486.6 eV). The pass energy of the spherical capacitor analyser was set at 35.75 eV. The energy scale of the photoelectron spectrometer was calibrated according to the ASTM standard procedure.[31] The photoelectron spectra were recorded with a step size of 0.2 eV and a dwell time of 5 seconds. The recorded C 1s photoelectron line was used to compensate for any charging effects and was set to the binding energy of 284.8 eV.[32]

The surface morphology of the annealed samples was observed with scanning electron microscopy (SEM) using a JEOL JSM-6500F (JEOL, Japan).

Grazing Angle X-ray diffractometry (GA-XRD) was used to identify the oxide phases present at the surface of the oxidized samples. The XRD patterns were recorded, with a Bruker D8 Discover diffractometer in the grazing incidence geometry using Co K_α radiation, in the 2θ region between 20 and 60 deg with a step size of 0.03 deg and a dwell time of 10 seconds. The incidence angle of the X-ray beam was fixed at 3 deg with respect to the sample surface.

To investigate the steel surface wettability, a Pb film of about 500 nm thick was deposited onto the surface of a second series of simultaneously annealed steel samples with a deposition rate of 0.15 nm/s corresponding to a power input of 20 W on the Pb target (99.99 pct, Chempur, Germany) in a Leica SCD500 sputter coater (Leica, Germany). Only the bare pure Fe, Fe–1.8 Mn and Fe–1.9 Mn–0.94 Si steel were sputtered clean in the Leica SCD500 sputter coater by an argon plasma to remove any adventitious air-borne species prior to the deposition of the Pb film.

After deposition of the Pb film, the samples were transferred to the quartz tube furnace again. Prior to heating up to 400 °C (above the melting point of Pb, i.e., beyond 327 °C) the furnace tube was flushed with Ar + 20 vol pct H_2 for 1 hour. Then, the sample was heated to 400 °C within 12 minutes and kept at this temperature for 10 minutes to let the Pb film form stable droplets on the surface; see Figure 1. During the

Table I.   Steel Composition in Weight Percent (Wt Pct)

Alloy	C	Mn	Si	Al
Fe–1.8 Mn	0.010	1.80	0.05	0.02
Fe–1.9 Mn–0.94 Si	0.104	1.90	0.94	0.017

Table II.   Oxygen Partial Pressure (pO_2) at 950 °C in Ar + 5 Vol Pct H_2 with Different Dew Points (DP)

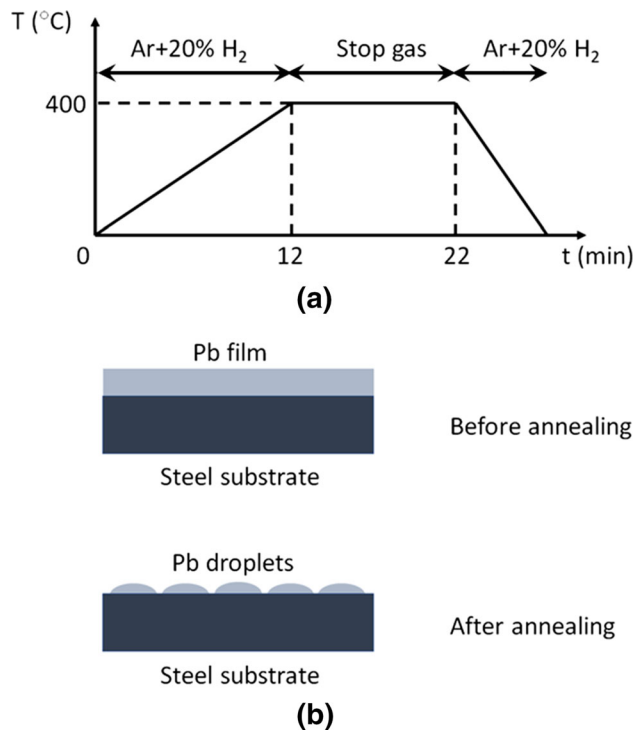| DP (°C)	− 40	− 30	− 10	0	+ 10
pO_2 (atm.)	2.5×10^{-21}	2.2×10^{-20}	1.0×10^{-18}	5.7×10^{-18}	2.3×10^{-17}

Fig. 1—(a) Temperature profile; and (b) schematic of de-wetting experiments.

holding time, the gas flow was stopped to avoid the destabilization of the droplets.

After rapid cooling, the Pb droplets were observed with SEM while the sample was tilted such that the sample surface normal made an angle of 70 deg with respect to the electron beam. The contact angle was obtained at the intersection of the circle shaped circumference with the chord connecting the droplet at the sample surface by ImageJ software with Contact Angle plug-in.[33] First, five points were selected on the contour line of the image of a Pb particle, two at the left and right contact angles and three at the droplet boundary. Next, an ellipse was fitted to the contour line of the droplets. Finally, the left and right contact angles were evaluated.[33]

Of some samples the contact angle of the Pb droplets were measured directly of cross-sections prepared by plasma focussed ion beam (PFIB) milling. To this end, scanning electron microscopy (SEM) combined with a Xenon plasma focused ion beam (Helios G4 PFIB UXe, Thermo Fisher Scientific, USA) was used. This instrument is equipped with an EDAX system (USA) for energy dispersive X-ray micro analysis (EDS) with Octane Elite plus detector using TEAM acquisition and analysis software (version 4.5). First, the surface of

the area of interest was covered with about 1 μm thick layer of Pt added with C. Next, a trench was cut with the PFIB operated at 30 keV. Then, the surface of the cross-section was polished with a low-current Xe ion beam.

III.   RESULTS AND DISCUSSION

A. Surface Oxides

Our previous studies[25,26] already showed that the oxides formed at the steel surface during annealing at high temperatures in relatively low oxygen partial pressure environments can be well predicted by thermodynamic calculations, as was validated by X-ray diffractometry (XRD). Apparently, local equilibrium exists between the steel surface and the annealing gas at high temperatures. Hence, the oxides present at the surface of Fe–1.8 Mn and Fe–1.9 Mn–0.94 Si after annealing can be assessed from the phase diagrams of Fe–Mn and Fe–Mn–Si alloys in an oxidizing environment at 950 °C; see Figure 2. These phase diagrams were constructed with FactSage using the thermodynamic data of the so-called solid solution oxides, (Fe,Mn)O, (Fe,Mn)$_2$SiO$_4$, (Fe,Mn)SiO$_3$ and SiO$_2$, in the FToxid database.[34] A solid solution of Fe–Mn binary and Fe–Mn–Si ternary alloy with fcc or bcc crystal lattice was created with the thermodynamic data in the FSstel database.[34] A gas mixture of Ar and O$_2$ with increasing oxygen partial pressure (in atm.) was created using the thermodynamic data in the FactPS database[35] to be in equilibrium with the alloy phase and the oxides.

The oxide phase that can be formed on a Fe–Mn binary alloy is considered as MnO and FeO; see Figure 2(a). Since both FeO and MnO have the same rock-salt crystal structure, FeO and MnO can form a continuous solid solution denoted as (Fe,Mn)O.[36] The Fe fraction in (Fe,Mn)O increases with oxygen partial pressure, which agrees with the results reported in Ref.[37] As confirmed by XRD analysis of the Fe–1.8Mn alloyed steel samples annealed at 950 °C with a DP ranging from − 40 °C to + 10 °C, (Fe,Mn)O is the dominant type of oxide formed. Due to the small amount of Si in the alloys (see Table I), traces of SiO$_2$ were formed. The lines in the diffractograms corresponding with (Fe,Mn)O shift to higher diffraction angles with increasing DP, indicating an increase of the fraction Fe in the oxide phase.

The oxide species formed on Fe–Mn–Si ternary alloys at 950 °C as a function of oxygen partial pressure and Si fraction in the range of 0–1.0 wt pct for a fixed Mn fraction of 1.9 wt pct can be predicted; see Figure 2(b). Adding Si to the Fe–Mn alloy leads to the formation of

SiO$_2$, (Fe,Mn)SiO$_3$ and (Fe,Mn)$_2$SiO$_4$. The oxides phases changes from SiO$_2$ to (Fe,Mn)SiO$_3$ and then to (Fe,Mn)SiO$_3$ + (Fe,Mn)$_2$SiO$_4$ and finally to (Fe,Mn)$_2$SiO$_4$ with increasing oxygen partial pressure. XRD analysis of the Fe–1.9 Mn–0.94 Si alloyed steel samples annealed at 950 °C with DP ranging from − 40 °C to + 10 °C shows that only some SiO$_2$ next to (Fe,Mn)SiO$_3$ is formed only at the lowest DP (− 40 °C) and with increasing DP more (Fe,Mn)$_2$SiO$_4$ is formed. This indicates that Fe fraction in the surface oxides increases with DP.
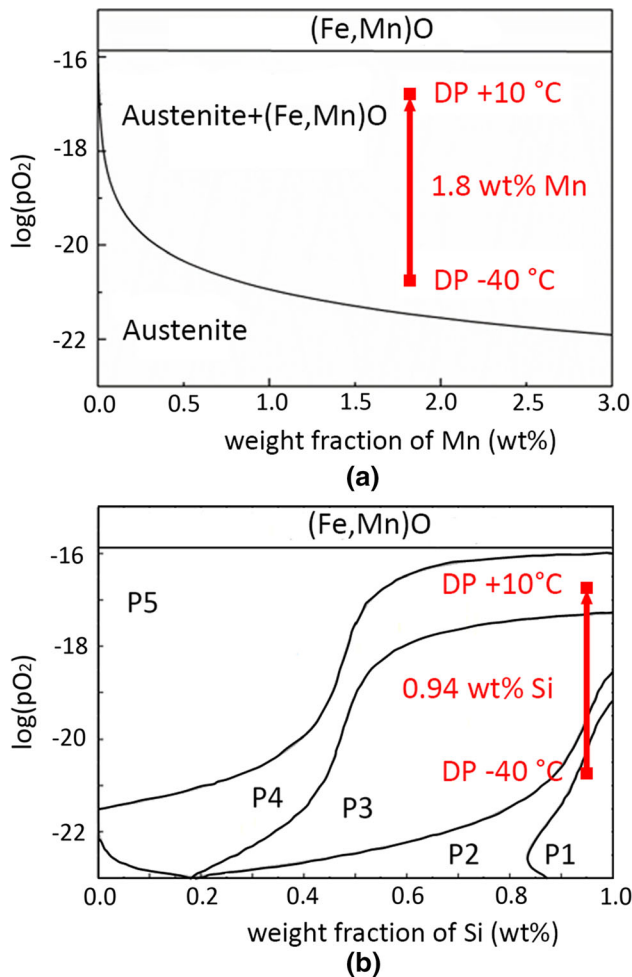
Fig. 2—Phase diagram computed with Factsage[35]: (a) Fe–Mn binary alloys at 950 °C in an oxidizing environment; (b) Fe–Mn–Si alloys with a fixed Mn fraction of 1.9 wt pct at 950 °C in an oxidizing environment. P1, P2, P3, P4, and P5 indicate SiO$_2$, (Fe,Mn)SiO$_3$, (Fe,Mn)$_2$SiO$_4$ + (Fe,Mn)SiO$_3$, (Fe,Mn)$_2$SiO$_4$, and (Fe,Mn)$_2$SiO$_4$ + (Fe,Mn)O correspondingly.

XPS analysis of the annealed steel surfaces showed that the Si 2p, Mn 2p$^3/_2$ and Fe 2p$^3/_2$ photoelectron lines are shifted to higher binding energies confirming that Si, Mn and Fe are bonded to oxygen at the surface; see Table III. No clear relation between the observed binding energies and the dew point of the annealing gas environment was observed. Since the differences in binding energies of Si 2p, Mn 2p$^3/_2$ and Fe 2p$^3/_2$ photoelectron lines for the various oxides are small (see[38]), the species composing the surface oxide layer could not be resolved unambiguously by curve fitting of the photoelectron spectra.

B. Surface Morphology and Composition

The morphology of the surface of Fe–1.8 Mn steels annealed at 950 °C for 1 hour in a mixture of Ar + 5 vol pct H$_2$ gases at dew points ranging from − 40 °C to + 10 °C are shown in Figures 3(a) through (e). The oxides identified as (Fe,Mn)O are dispersed at the surface or decorate the grain boundaries after annealing at each dew point. According to XPS analysis, the intensity of the oxidic component of the Fe 2p lines (binding energy of about 710 eV) increases with increasing dew point and hence the Fe fraction in (Fe,Mn)O increases with increasing dew point in agreement with thermodynamic predictions[37]; see Figures 4(a) and (b). Internal oxidation is promoted with increasing DP, which also can be seen in Figures 5(a) and (b). The size of precipitates close to the surface tends to be larger than those at inner region and near grain boundaries.

The surface morphologies of the Fe–1.9 Mn–0.94 Si steels annealed at 950 °C for 1 hour in a mixture of Ar + 5 vol pct H$_2$ gases at dew points ranging from − 40 °C to + 10 °C are shown in Figures 3(f) through (j). Oxides are visible on the surface of each sample annealed at different dew points. The oxides on the surface of annealed Fe–1.9 Mn–0.94 Si steel samples are identified as SiO$_2$, (Fe,Mn)SiO$_3$, (Fe,Mn)$_2$SiO$_4$ according to the oxide phase diagram [cf. Figure 2 (b)] and in agreement with XRD and XPS; see Figure 4(c). Also, for this steel alloy it was observed with XPS that the fraction of Fe in the oxides depends on the dew point of the annealing ambient; see Figure 4(d). The intensity of the oxidic component of the Fe 2p lines increases with increasing dew point; see also Figure 4(c). Even, at a dew point of − 40 °C no Fe was detected in the surface oxide. Internal oxidation is promoted with increasing DP of the annealing ambient for the Fe–1.9 Mn–0.94 Si alloy; see Figures 5(c) and (d). But an oxide film is present after annealing at all dew points ranging from − 40 °C to + 10 °C. The addition of Si enhances external oxidation and formation of Si-rich oxides along the grain boundaries.

Table III. Binding Energies of the Photoelectron Lines Measured with XPS of the Annealed Steel Surfaces

Alloy	O 1s (eV)	Si 2p (eV)	Mn 2p$^3/_2$ (eV)	Fe 2p$^3/_2$ (eV)	Oxide Phases
Fe–1.8 Mn	530.0 ± 0.1	101.5 ± 0.3	641.2 ± 0.2	710.3 ± 0.2	(Fe,Mn)O/SiO$_2$
Fe–1.9 Mn–0.94 Si	530.9 ± 0.1	101.6 ± 0.3	641.6 ± 0.1	710.5 ± 0.2	SiO$_2$/(Fe,Mn)SiO$_3$/(Fe, Mn)$_2$SiO$_4$
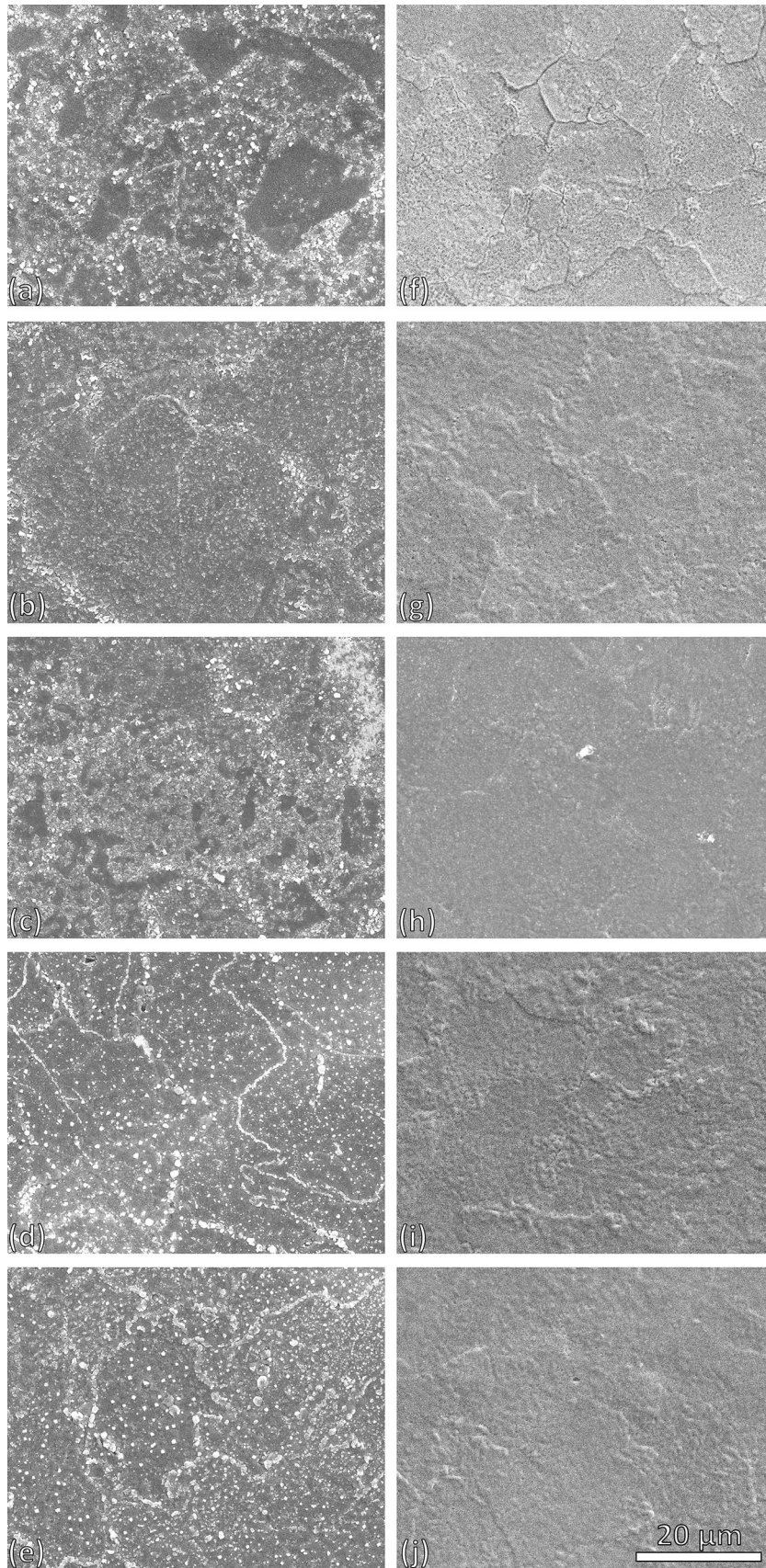
C. *Contact Angle of Pb Droplets*

The wettability of the various steel surfaces after annealing was investigated by de-wetting of a Pb film applied by sputter deposition; cf. Figure 1. The contact angle was determined from the Pb droplets after rapid solidification as observed with SEM; see Figure 6. For each steel surface, 10 droplets were selected to measure the contact angle. The average and standard deviation of the measured contact angles as a function of the DP of the annealing gas ambient are presented in Figure 7.

After annealing of both Fe–1.8 Mn and Fe–1.9 Mn–0.94 Si steels, the contact angle of Pb droplets after de-wetting of a Pb film basically tends to decrease with increasing dew point of the annealing gas as can be seen in Figure 7. This decrease of the contact angle suggests an improved wettability with increasing dew point. As has been demonstrated, internal rather than external oxidation is promoted when increasing dew point of the

annealing gas. But also, the fraction of Fe in the surface oxide increases with increasing dew point of the annealing gas; see Figures 4(b) and (d).

If promoting internal oxidation would contribute to less surface oxides, then that would certainly be favourable for wetting the surface and consequently beneficial coating adhesion. In the case of de-wetting a Pb film on the steel surfaces after annealing with surface oxides present, the effect of oxide composition may be dominant.

The thermodynamic work of adhesion between a liquid droplet on a solid surface according to the Young-Dupré equation modified for the so-called spreading pressure π_e can be written as[39,40]:

$$WoA = (1 + \cos\theta_Y)\gamma_{lv} + \pi_e, \qquad [1]$$

where θ_Y is the contact angle and γ_{lv} is the surface energy at the liquid–vapour interface. Thus, the WoA can be directly related to contact angle, which is a measure of the surface wettability. The WoA has been calculated for interfaces between liquid Pb and different oxides as well as between liquid Pb and Fe; see Table IV. The method used to calculate the WoA is explained
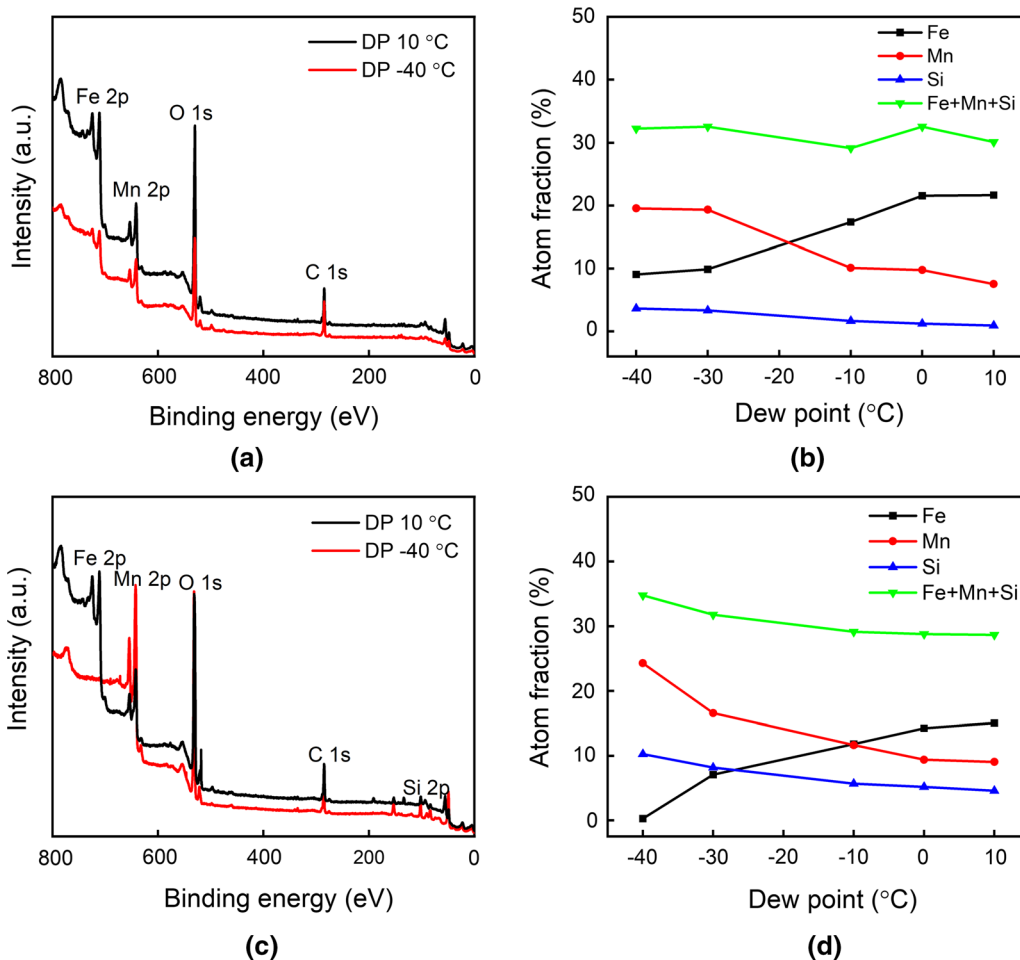

Fig. 4—X-ray photoelectron spectrum acquired from the surface of (*a*) Fe–1.8 Mn steel and (*c*) Fe–1.9 Mn–0.94 Si steel annealed for 1 h at 950 °C in a mixture of Ar + 5 vol pct H₂ at dew points − 40 °C and + 10 °C; and the atom fraction of each element bonded to oxygen at the surface of (*b*) Fe–1.8 Mn steel and (*d*) Fe–1.9 Mn–0.94 Si steel annealed at different dew point.
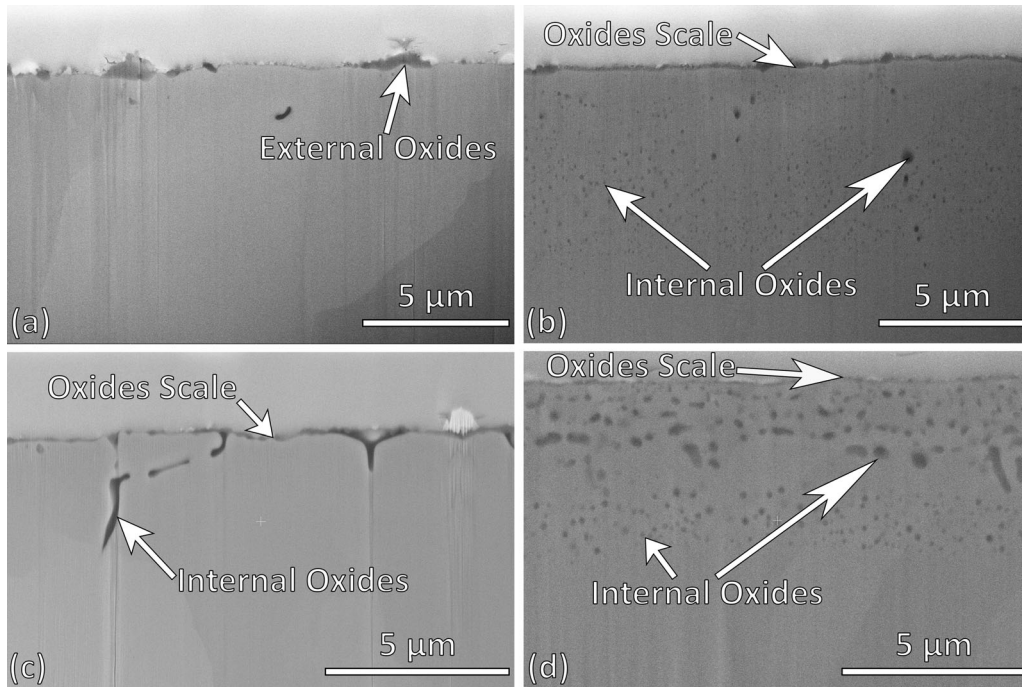
Fig. 5—SEM images of the cross-section of Fe–1.8 Mn steel annealed at dew points (a) − 40 °C and (b) + 10 °C; and Fe–1.9 Mn–0.94 Si steel annealed at dew points (c) − 40 °C and (d) + 10 °C for 1 h at 950 °C in a mixture of Ar + 5 vol pct H_2.
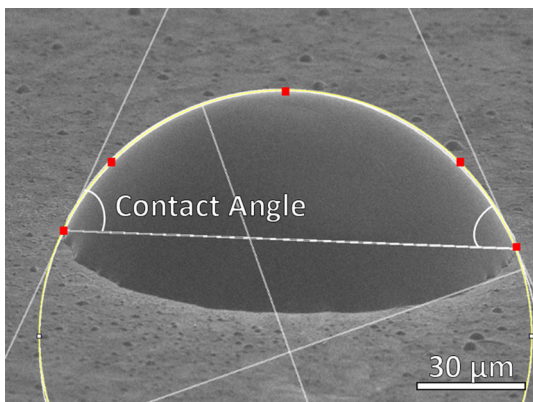

Fig. 6—SEM image of Pb droplets on Fe–1.9 Mn–0.94 Si steel annealed at DP − 40 °C. The sample surface normal is tilted by 70 deg with respect to the electron beam. The red squares indicate the selected points on the contour line of the Pb droplet for image analysis, the yellow curve indicate the ellipse used to fit the contour line (Color figure online).

elsewhere.[17,41,42] For comparison also the *WoA* between liquid Zn and these interfaces has been determined, which is relevant for galvanising of steel. A similar trend as for Pb holds for Zn.

The main difference between wetting the same surface with liquid Pb and Zn is their surface energy at the liquid–vapour interface γ_{lv}, which equals 0.457 and 0.789 J/m^2, respectively, at the melting point of Pb (327 °C) and Zn (420 °C), respectively.[43] Thus, the contact angle of a Pb droplet will be smaller than that of a Zn droplet (without reactive wetting) on the same surface.

The liquid droplet is also in equilibrium with its vapour. This vapour adsorbs at the surface next to the droplet and consequently effect the surface energy of the solid substrate. For example, from the observed contact angle of Pb droplets on pure Fe (see Table V and Figure 8(a)), the spreading pressure according to Eq. [1] equals 1.7 J/m^2.

The higher *WoA* for FeO compared with that of SiO_2 and MnO supports the trend observed for the measured contact angle as a function of dew point; see Figure 7. Since the amount of Fe in the oxide increases with increasing dew point (cf. Figures 4(b) and (d)), and similarly the measured contact angle decreases with increasing dew point, the *WoA* according to Eq. [1] increases with increasing dew point.

Furthermore, the contact angle of the Pb droplets on annealed Fe–1.9 Mn–0.94 Si steels is significantly higher than those on Fe–1.8 Mn, which suggests that the wettability of the steel with Si is poorer. This corresponds well with the lower *WoA* for SiO_2/Pb compared with that of MnO/Pb and FeO/Pb; see Table IV. The amount of Si bonded to oxygen at the steel surface only slightly decreases with increasing of the dew point in the range considered in this study; see Figure 4(d).

The contact angles of Pb on bare pure Fe, Fe–1.8 Mn and Fe–1.9 Mn–0.94 Si steel surfaces with no oxides were also measured; see Table V. For comparison, these contact angles were also measured directly from cross-sections prepared with PFIB; see Figure 8. From the values reported in Table V, it can be concluded that these contact angles are comparable with the contact angles determined by the image analysis method, but systematically smaller (5 to 8 deg). The contact angles for the steels surfaces without any oxides are somewhat
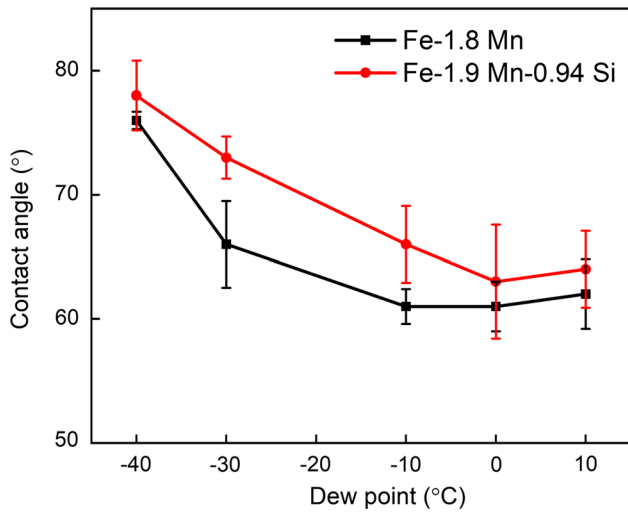
Fig. 7—Contact angle of Pb droplets after de-wetting of Pb film on Fe–1.8 Mn steel and Fe–1.9 Mn–0.94 Si steel annealed at different dew points. Each data point represents the average contact angle of measuring10 droplets.

Table IV. Work of Adhesion (*WoA*) for Interfaces Between Liquid Pb or Zn and Different Oxides as well as Pure Fe

Interface	WoA (J/m^2)
Pb/Fe	2.50
Pb/FeO	1.82
Pb/MnO	1.43
Pb/SiO$_2$	1.10
Zn/Fe	3.20
Zn/FeO	2.67
Zn/MnO	2.16
Zn/SiO$_2$	1.94

Table V. Contact Angle of Pb Droplets on Bare Surfaces as Determined by ImageJ Method and from PFIB Cross Sections

Sample	ImageJ (deg)	PFIB (deg)
Fe	46.9 ± 2.2	41.7
Fe–1.8 Mn	59.3 ± 2.5	51.6
Fe–1.9 Mn–0.94 Si	59.7 ± 5.3	51.9

lower than those on steels with oxides on the surfaces, but close to those of the steels annealed at high dew point; cf. Figure 7. This supports the idea that good wettability of these steels is achieved by annealing in a gas ambient with at relatively high dew point. The smallest contact angle is observed for the Pb droplets on bare pure Fe. This shows the effect of the alloying elements Mn and Si on the *WoA*, in agreement with earlier predictions.[44] Thus, the best wettability occurs
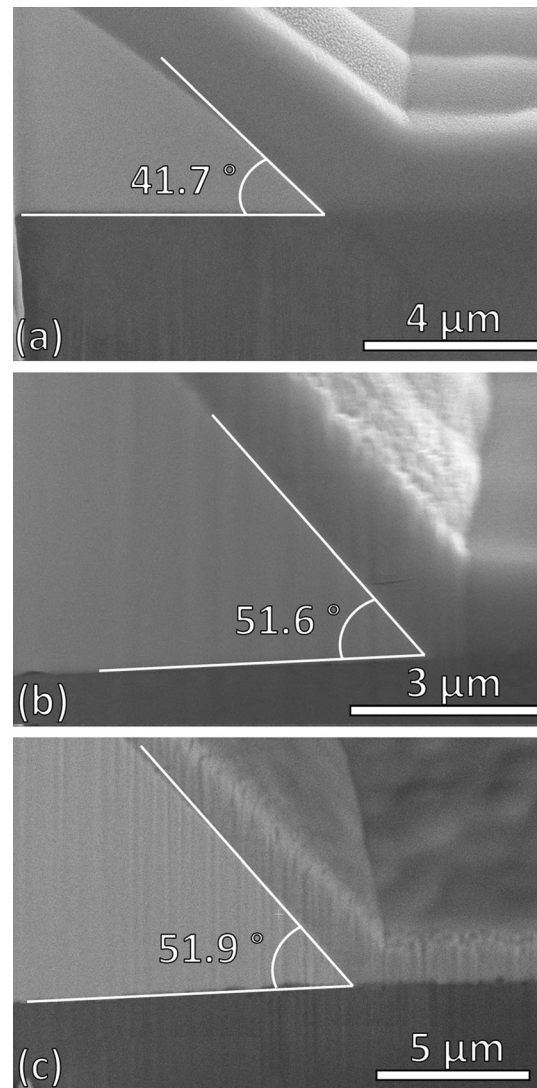

Fig. 8—Contact angles of Pb droplets on oxide free surface of (*a*) pure Fe, (*b*) Fe–1.8 Mn steel, and (*c*) Fe–1.9 Mn–0.94 Si steel as determined from cross sections prepared by PFIB.

when no oxides and alloying elements Mn and Si are present at the surface.

IV. CONCLUSIONS

After annealing Fe–1.8 Mn and Fe–1.9 Mn–0.94 Si steels at 950 °C in an Ar + 5 vol pct H$_2$ gas flow with a dew point ranging from − 40 °C to + 10 °C, oxides were observed along the grain boundaries or dispersed on the surface for the Fe–1.8 Mn steel, while a continuous oxides layer was formed on Fe–1.9 Mn–0.94 Si steel. (Fe,Mn)O was formed on the surface of Fe–1.8 Mn steel. SiO$_2$ were formed on the surface of Fe–1.9 Mn–0.94 Si steel after annealing with low dew points, while (Fe,Mn)SiO$_3$ and/or (Fe,Mn)$_2$SiO$_4$ after annealing with high dew points. For both steels it holds that the Fe fraction in the surface oxides increases with increasing dew point. Addition of Si enhances external

oxidation and formation of oxides along grain boundaries.

The presence of surface oxides on the steels reduces their wettability. The contact angle of Pb droplets on the steel surfaces after annealing decreases and thus the wettability increases with increasing dew point due to an increasing amount of Fe in the surface oxides. The presence of Si in the surface oxide further reduces the wettability.

CONFLICT OF INTEREST

On behalf of all authors, the corresponding author states that there is no conflict of interest.

REFERENCES

1. J. Mahieu, S. Claessens, and B.C. De Cooman: *Metall. Mater. Trans. A*, 2001, vol. 32A, pp. 2905–08.
2. L. Cho, S.J. Lee, M.S. Kim, Y.H. Kim, and B.C. De Cooman: *Metall. Mater. Trans. A*, 2013, vol. 44, pp. 362–71.
3. R. Khondker, A. Mertens, and J.R. McDermid: *Mater. Sci. Eng. A*, 2007, vol. 463, pp. 157–65.
4. B. Mintz: *Int. Mater. Rev.*, 2001, vol. 46, pp. 169–97.
5. M. Kim, J. Kwak, J. Kim, Y. Liu, N. Gao, and N.Y. Tang: *Metall. Mater. Trans. A*, 2009, vol. 40A, pp. 1903–10.
6. G.M. Song, T. Vystavel, N. van der Pers, J.T.M. De Hosson, and W.G. Sloof: *Acta Mater.*, 2012, vol. 40, pp. 2973–81.
7. A. Marder: *Prog. Mater. Sci.*, 2000, vol. 45, pp. 191–271.
8. L. Chen, H.S. Kim, S.K. Kim, and B.C. De Cooman: *ISIJ Int.*, 2007, vol. 47, pp. 1804–12.
9. Q. Tonizzo, A.F. Gourgues-Lorenzon, M. Mazière, A. Perlade, and I. Zuazo: *Mater. Sci. Eng. A*, 2017, vol. 706, pp. 217–26.
10. S. Alibeigi and J.R. McDermid: in *Materials Science and Technology Conference and Exhibition 2012, MS and T 2012*, 2012, pp. 147–54.
11. E.M. Bellhouse and J.R. McDermid: *Metall. Mater. Trans. A*, 2011, vol. 42A, pp. 2753–68.
12. E.M. Bellhouse and J.R. McDermid: *Metall. Mater. Trans. A*, 2012, vol. 43A, pp. 2426–41.
13. M.L. Giorgi, J. Diawara, S. Chen, A. Koltsov, and J.M. Mataigne: *J. Mater. Sci.*, 2012, vol. 47, pp. 8483–95.
14. S. Jiang, S. Feng, X. Yuan, Y. Li, Z. Li, and Q. Zhang: *J. Iron. Steel Res. Int.*, 2014, vol. 21, pp. 1059–64.
15. Y. Kim, K. Shin, S. Jeon, K. Chin, and J. Lee: *Corros. Sci.*, 2014, vol. 85, pp. 364–71.
16. I. Hertveldt, B.C. De Cooman, and S. Claessens: *Metall. Mater. Trans. A*, 2000, vol. 31A, pp. 1225–32.
17. G.M. Song, W.G. Sloof, T. Vystavel, and J.T.M. De Hosson: *Mater. Sci. Forum*, 2007, vol. 539–543, pp. 1104–09.
18. A. Mertens, E.M. Bellhouse, and J.R. McDermid: *Mater. Sci. Eng. A*, 2014, vol. 608, pp. 249–57.
19. S. Alibeigi, R. Kavitha, R.J. Meguerian, and J.R. McDermid: *Acta Mater.*, 2011, vol. 59, pp. 3537–49.
20. R. Kavitha and J.R. McDermid: *Surf. Coat. Technol.*, 2012, vol. 212, pp. 152–58.
21. M.L. Giorgi and A. Koltsov: in *Galvatech 2017*, Tokyo, Japan, 2017.
22. M.L. Giorgi, J. Diawara, M. Rivollier, H. Duval, and A. Koltsov: *ISIJ Int.*, 2018, vol. 58, pp. 1592–99.
23. M. Pourmajidian and J.R. McDermid: *Surf. Coat. Technol.*, 2019, vol. 357, pp. 418–26.
24. V.A. Lashgari, C. Kwakernaak, and W.G. Sloof: *Oxid. Met.*, 2014, vol. 81, pp. 435–51.
25. W. Mao, R.W. Hendrikx, and W.G. Sloof: *Oxid. Met.*, 2018, vol. 89, pp. 531–49.
26. W. Mao, Y. Ma, and W.G. Sloof: *Oxid. Met.*, 2018, vol. 90, pp. 237–53.
27. J. Moon, J. Lowekamp, P. Wynblatt, S. Garoff, and R.M. Suter: *Surf. Sci.*, 2001, vol. 488, pp. 73–82.
28. Z. Shi and P. Wynblatt: *Metall. Mater. Trans. A*, 2002, vol. 33A, pp. 2569–72.
29. Z. Wang, P. Wynblatt, and D. Chatain: *Interface Sci.*, 1999, vol. 7, pp. 173–80.
30. D. Huin, P. Flauder, and J.B. Leblond: *Oxid. Met.*, 2005, vol. 64, pp. 131–67.
31. American society for testing and materials. Standard practice for checking the operating characteristics of X-ray photoelectron spectrometers (E902-88). *Surf. Interface Anal.*, 1991, vol. 17, pp. 889–92.
32. T.L. Barr: *Modern ESCA: the Principles and Practice of X-Ray Photoelectron Spectroscopy*, CRC Press, Boca Raton, 1994.
33. P. Buahom: Measuring the Contact Angle Using ImageJ with Contact Angle Plug-in (ResearchGate, 2018), https://www.researchgate.net/publication/328733959, accessed 05 November 2007.
34. Y.F. Gong and B.C. De Cooman: *Steel Res. Int.*, 2011, vol. 82, pp. 1310–18.
35. Factsage Database Documentation : http://www.crct.polymtl.ca/fact/documentation/, accessed 26 January 2021.
36. P. Franke and R. Dieckmann: *J. Phys. Chem. Solids*, 1990, vol. 51, pp. 49–57.
37. W. Mao and W.G. Sloof: *Scr. Mater.*, 2017, vol. 135, pp. 29–32.
38. A.P. Grosvenor, E.M. Bellhouse, A. Korinek, M. Bugnet, and J.R. McDermid: *Appl. Surf. Sci.*, 2016, vol. 379, pp. 242–48.
39. W.D. Kaplan, D. Chatain, P. Wynblatt, and W.C. Carter: *J. Mater. Sci.*, 2013, vol. 48, pp. 5681–5717.
40. R.J. Good: *J. Colloid Interface Sci.*, 1975, vol. 52, pp. 308–13.
41. I.J. Bennett, J.M. Kranenburg, and W.G. Sloof: *J. Am. Ceram. Soc.*, 2005, vol. 88, pp. 2209–16.
42. C. Kwakernaak and W.G. Sloof: *Ceram. Int.*, 2018, vol. 44, pp. 23172–79.
43. B.J. Keene: *Int. Mater. Rev.*, 1993, vol. 38, pp. 157–92.
44. G.M. Song and W.G. Sloof: *Surf. Coat. Technol.*, 2011, vol. 205, pp. 4632–39.